PASJ: Publ. Astron. Soc. Japan 61, S17–S33, 2009 January 30

Modeling and Reproducibility of Suzaku HXD PIN/GSO Background

Yasushi FUKAZAWA,[1] Tsunefumi MIZUNO,[1] Shin WATANABE,[2] Motohide KOKUBUN,[2] Hiromitsu TAKAHASHI,[1] Naomi KAWANO,[1] Sho NISHINO,[1] Mahito SASADA,[1] Hirohisa SHIRAI,[1] Takuya TAKAHASHI,[1] Yudai UMEKI,[1] Tomonori YAMASAKI,[1] Tomonori YASUDA,[1] Aya BAMBA,[2] Masanori OHNO,[2] Tadayuki TAKAHASHI,[2] Masayoshi USHIO,[2] Teruaki ENOTO,[3] Takao KITAGUCHI,[3] Kazuo MAKISHIMA,[3,4] Kazuhiro NAKAZAWA,[3] Yuichi UEHARA,[3] Shin'ya YAMADA,[3] Takayuki YUASA,[3] Naoki ISOBE,[4] Madoka KAWAHARADA,[4] Takaaki TANAKA,[5] Makoto S. TASHIRO,[6] Yukikatsu TERADA,[6] and Kazutaka YAMAOKA[7]

[1]*Department of Physical Science, Hiroshima University, 1-3-1 Kagamiyama, Higashi-Hiroshima, Hiroshima 739-8526*
fukazawa@hirax7.hepl.hiroshima-u.ac.jp

[2]*Department of High Energy Astrophysics, Institute of Space and Astronomical Science (ISAS), Japan Aerospace Exploration Agency (JAXA), 3-1-1 Yoshinodai, Sagamihara, Kanagawa 229-8510*

[3]*Department of Physics, University of Tokyo, 7-3-1 Hongo, Bunkyo, Tokyo 113-0033*

[4]*Cosmic Radiation Laboratory, The Institute of Physical and Chemical Research (RIKEN), 2-1 Hirosawa, Wako, Saitama 351-0198*

[5]*SLAC National Accelerator Laboratory and KIPAC, Stanford University, Menlo Park, CA 94025, USA*

[6]*Department of Physics, Saitama University, 255 Shimo-Ohkubo, Saitama-City, Saitama 338-8570*

[7]*Department of Physics, Aoyama Gakuin University, 5-10-1 Fuchinobe, Sagamihara, Kanagawa 229-8558*

(Received 2008 July 23; accepted 2008 November 11)

Abstract

Suzaku Hard X-ray Detector (HXD) achieved the lowest background level than any other previously or currently operational missions sensitive in the energy range of 10–600 keV, by utilizing PIN photodiodes and GSO scintillators mounted in BGO active shields to reject particle background and Compton-scattered events as much as possible. Because it does not have an imaging capability nor rocking mode for the background monitor, the sensitivity is limited by the reproducibility of the non X-ray background (NXB) model. We modeled the HXD NXB, which varies with time as well as other satellites with a low-Earth orbit, by utilizing several parameters, including particle monitor counts and satellite orbital/attitude information. The model background is supplied as an event file in which the background events are generated by random numbers, and can be analyzed in the same way as the real data. The reproducibility of the NXB model depends on the event selection criteria (such as cut-off rigidity and energy band) and the integration time, and the 1 σ systematic error is estimated to be less than 3% (PIN 15–40 keV) and 1% (GSO 50–100 keV) for more than 10 ks exposure.

Key words: instrumentation: detectors — methods: data analysis — X-rays: general

1. Introduction

The hard X-ray detector (HXD) (Takahashi et al. 2007; Kokubun et al. 2007) onboard Suzaku (Mitsuda et al. 2007) has been developed to enable observations of astronomical objects with a good sensitivity in the 10–600 keV band. When the HXD data are combined with data from the X-ray CCD camera (XIS), they simultaneously cover a wide energy band, from 0.2 keV to 600 keV. The HXD sensor part (HXD-S) consists of 64 Si-PIN photo diodes and 16 GSO/BGO phoswich counters, shielded by 20 BGO anti-coincidence counters. Such a compound-eye configuration greatly reduces the background and the dead-time. Each of the phoswich counter (well counter) units includes 4 Si-PIN photo diodes with 2 mm thickness and 4 GSO scintillators with 5 mm thickness, located at the bottom of the BGO well-shaped active collimator. The HXD is the first astronomical detector to utilize such thick Si-PIN diodes and high-Z GSO scintillators. In order to achieve a lower background level than any other previous missions, the HXD has been designed to contain fewer radio isotopes — which may be naturally contained in the detector or activated in the orbit — and reject background events very effectively. The important goal of the HXD is to achieve a low background level by rejecting particle background and Compton-scattered events as much as possible. It has been found that, considering the detection efficiency, the residual background level of the HXD has become 10 mCrab at 20 keV and 1 Crab at 200 keV, the lowest of all previous missions, such as BeppoSAX and RXTE. Such a low background level enables us to detect weak sources of several hundred μCrab in the several tens keV band or several mCrab around 100 keV, without a necessity for "rocking motion" of the detector for simultaneous monitoring of the background, as has been done with CGRO / OSSE, BeppoSAX / PDS, and RXTE / HEXTE.

Such a low background level and narrow field of view are unique in order to permit the detection of faint hard sources, cause less source confusion and contribution of the Cosmic X-ray Background, and provide a rudimentary capability to study the structure for the emission region of hard X-rays, especially for supernova remnants, galactic diffuse X-ray emission, and galaxy clusters. Simultaneous observations with the XIS CCD camera – with no gap in the spectral coverage – are

Table 1. Acronym.

HXD	Hard X-ray Detector
PIN	p-i-n type Si photo diode in the HXD
GSO	$Gd_2SiO_5(Ce)$ scintillator in the HXD
BGO	$Bi_4Ge_3O_{12}$ anti-coincidence scintillator in the HXD
BGD	background
CXB	Cosmic X-ray background
NXB	non X-ray background
SAA	South Atlantic Anomaly
PINUD	PIN Upper discriminate counter
$PINUD_{buildup}$	convolution of PINUD with an exponential decay function
COR	geomagnetic cut-off rigidity
PINUDLCUNIT (bgd_a or quick)	background model (subsection 3.1)
LCFITDT (bgd_d or tuned)	background model (subsection 3.2)
LCFIT	background model (subsection 3.2)
GSOHCNT	count rate of GSO event in 450–700 keV
GLC	gradually increasing component of the GSO background event in 450–700 keV
T_SAA_HXD	elapsed time after the SAA

very effective to constrain the time variability of the broad-band spectrum, and the appreciable effective area up to several hundred keV enables us to determine the continuum shape accurately, which is especially important for time-variable galactic binaries and active galaxies.

Although the HXD achieved a low background level, the count rate of the background significantly varies with time, depending on mainly two parameters: the geomagnetic cut-off rigidity (COR) and the elapsed time after passages of the South Atlantic Anomaly (SAA), but weak dependences on other parameters, such as Earth elevation, are found. Therefore, the NXB must be estimated by taking into account these dependences. Since the sensitivity is limited by the reproducibility of the NXB, a correct NXB model is strongly required. The HXD team has developed its NXB model with several different methods and unified them by combining the advantages of each method. Here we report on the HXD background modeling and its reproducibility. Corresponding Suzaku documents are also available on the Suzaku web site as Suzaku memo[1] 2007-01, 2007-02, 2007-09, 2008-01, and 2008-03. In this paper, some technical terms often appear, and therefore we summarize them in table 1.

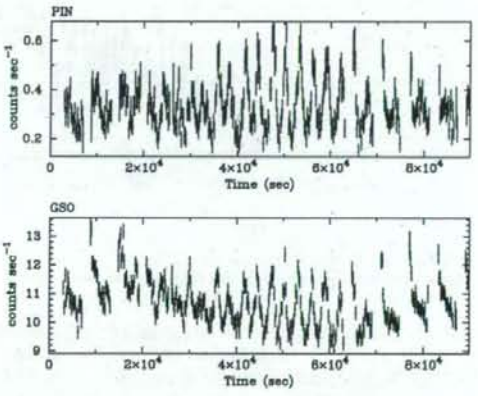

Fig. 1. Top and bottom show examples of light curves of the PIN (15–40 keV) and GSO (50–200 keV) background, respectively. The variation of COR-dependence is seen at $(2–6) \times 10^4$ s, and exponential-decay components after passages of SAA are seen at $(0–2) \times 10^4$ s and after 6×10^4 s.

2. Characteristics of HXD NXB

Here, we describe the characteristics of the HXD NXB. We utilize the data during Earth occultation, which are almost equivalent to the NXB. The Earth albedo is at most 10% of the CXB flux below 50 keV (Imhof et al. 1976; Churazov et al. 2007; Frontera et al. 2007; Sazonov et al. 2007; Churazov et al. 2008), and the CXB flux is 5% of the PIN NXB and $<0.5\%$ of the GSO NXB.

2.1. *Summary of the NXB Components*

A detailed description of the HXD NXB was written in Kokubun et al. (2007). Here, we shortly review it, and present characteristics that have been newly found. An example of light curves of the HXD background is shown in figure 1. The HXD background events are mainly caused by natural radioactive isotopes, SAA-induced radio isotopes, primary and secondary cosmic rays, and atmospheric albedo neutrons. Therefore, the count rate of the background significantly varies with time, depending on mainly two parameters. First is the dependence of the COR for primary cosmic rays and atmospheric neutrons. This dependence is well tracked by PINUD, which counts the upper discriminator signal of the PIN at a threshold energy of ~ 90 keV. Therefore, the PINUD is insensitive to X-ray events, but monitors the flux of real-time charged particles. Since the PIN diodes are embedded in the thick BGO shields, PINUD counts the protons above

[1] (http://www.astro.isas.jaxa.jp/suzaku/doc/).

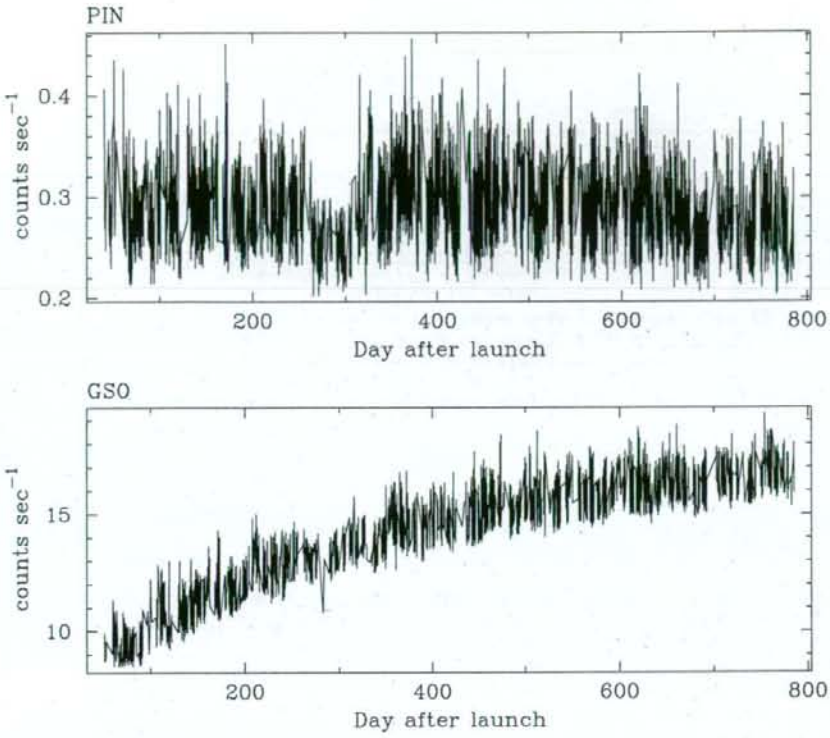

Fig. 2. Time history of the PIN count rate (15–40 keV) (top) and the GSO count rate (50–200 keV) (bottom) of NXB during Earth occultation data. The period of the low count rate of the PIN NXB corresponds to 2006/03/23–2006/05/13 (day from launch = 256–307).

$\sim$ 100 MeV. This component is dominant in the variation of PIN NXB and GSO NXB below 140 keV. The spectra of PIN NXB become harder as the COR decreases or the PINUD increases. The PINUD is considered to be a better indicator of the particle flux than the COR, because the particle environment against the COR would depend on the solar activity. The second is exponential-decay components after passages of SAA, due to the activated material bombarded by SAA protons, which is monitored by the hit count of PINUD integrated during the SAA (thus representing the total accumulated dose). This component is significant in the GSO band below 100 keV and above 400 keV, while the variation due to this component is smaller for the PIN NXB. Since there are many activated nuclides with different lifetimes, many time scales of NXB variation also exist in the range of several seconds to several hundred days. These two dependences are the clearest, but other weak dependences have been found. For example, the background rate is somewhat dependent on whether the pointing direction is toward the sky or Earth. Details are described later in sub-subsection 3.2.3.

2.2. *HXD Operation and NXB*

Apart from the intraday variation, the count rate of the NXB depends on the HXD operation mode and activation of the detector material with long lifetimes. There has been two kinds of important changes of the HXD operation mode. The lower discrimination level and pulse-shape discrimination level for the GSO signal determines the background rejection efficiency of PIN NXB, and therefore their level change can cause a change of the PIN NXB. Due to the noise increase of one PIN, possibly caused by the in-orbit radiation damage, the bias high voltage to the PIN was changed twice. Since the thickness of the depletion layer depends on the bias, this change slightly affected the energy response of the 16/32 PIN, and thus the PIN NXB rate might also be affected. Therefore, the response matrices corresponding to different bias voltages were supplied from the HXD team. The activation due to long-lived radioactive nuclei leads to an increase of the NXB rate, especially for the GSO.

Here, we discuss the long-term variation of the NXB, concerning the above issues. Figure 2 top shows a two-year history of the PIN NXB count rate (15–40 keV) during Earth occultation data. The count rate is almost constant, and thus the activation is not important for the PIN NXB. However, some discrete or gradual changes are seen; the most significant are two discrete jumps around days 260 and 310. This is due to the above level changes for the GSO on 2006 March 23 and May 13. The bias voltages for 16 out of 64 PIN were reduced

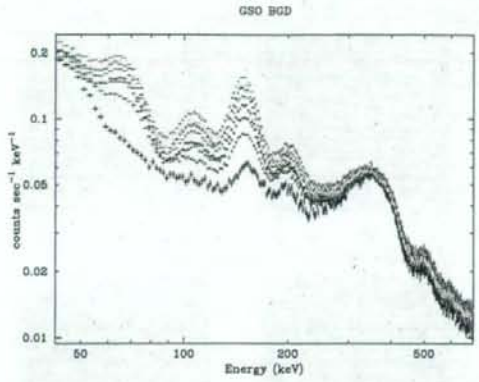

Fig. 3. Comparison of the GSO NXB spectra using Earth occultation data in different epochs; 2005-08-31, 2005-12-03, 2006-03-09, 2006-06-13, 2006-09-26, 2007-01-05, 2007-04-10, and 2007-08-09 from bottom to top.

from 500 V to 400 V on 2006 May 29 (323 days after the launch), and those of additional 16 PIN down to 400 V on 2006 October 3 (450 days after the launch). Nevertheless, we find no significant changes of the PIN NXB rate from this figure. Apart from those variations, the PIN NXB rate will suffer from an increase of solar activity in the near future.

In figure 2 bottom, a two-year history of the GSO count rates of the NXB in 50–200 keV during Earth occultation data is plotted. Due to the activation of long-lived nuclides during the SAA passage, the count rate gradually increases, and is reaching saturation. The increase is larger in the lower energy band. Figure 3 shows a comparison of spectra of Earth occultation data in different epochs. Gradual increases of several activation-induced lines are clearly seen. During 2006 March 14 to May 13 (247–307 days after the launch), the observational mode for the GSO was changed several times to optimize the setting parameters before the guest observer program started. The GSO count rate below 100 keV, especially around the lower discri level, was affected by these mode changes. Although this affection is significant, but small, it is not clearly seen in figure 3. As a result, the background model should consider these issues.

3. Modeling of NXB

The most ideal model of the NXB is based on a first principle: predicting the NXB count rate by considering the orbital particle environment and the detector response correctly, for example, by Monte-Carlo simulations. We in fact predicted the GSO background level due to activation by Monte-Carlo simulations (Kokubun et al. 1999; Kokubun et al. 2007) within a factor of 2. However, in order to reproduce the NXB with a few percent accuracy, it is more realistic to utilize the actually observed NXB. In that case, there are usually two types of methods.

One is based on the NXB data base, which is sorted by some parameters, such as COR, and the NXB for the observation is constructed by referring to parameters to extract the data base. This method is available when the number of sorting parameters is at most two; the NXB time variation is not so complex. Furthermore, it is needed that the background properties, which would depend on other parameters than sorting parameters, do not change within the period during which the NXB data base is accumulated. The background model of the Suzaku XIS applies this method (Tawa et al. 2008). However, strictly speaking, the NXB usually depends on more than two parameters, and therefore the accuracy of this method is somewhat limited.

The second method is to predict the NXB by an empirical function that represents the NXB time variation by several parameters. The function is constructed through an analysis of the real-time variation of the NXB. The background models of the Ginga LAC and the RXTE PCA are based on this method (Hayashida et al. 1989; Jahoda et al. 2006). This method can include many parameters to represent the function, but sufficient statistics of the NXB is necessary to track the time variation of NXB with a time scale of several hundred seconds. In the case of a low count rate of NXB, it is somewhat difficult to find modeling parameters.

The count rate of the PIN NXB is not very high, but enough to utilize the second method, while that of the GSO NXB is high and more variable. The latter method is more accurate, but cannot prepare the NXB model just after the data becomes available, while the former method can prepare the NXB model quickly. Therefore, we developed the PIN NXB model using both methods and the GSO NXB model using only the latter one. The model background is supplied as an event file by generating the background event by random numbers, and can be analyzed in the same way as a real event file.

3.1. *Method Based on the Data Base Sorted by PINUD and PINUD Build-Up:* `PINUDLCUNIT` *(PIN NXB model)*

The method described here utilizes the two-parameter-sorted data base, and is applied to the PIN NXB model. In this method (`PINUDLCUNIT`),[2] the NXB model is constructed on the data base of the Earth occultation data. The real-time PINUD count rate can be used as a good indicator of the NXB component. Another NXB component related to activation cannot be modeled by simply using PINUD. Therefore, we introduced a parameter, "PINUD build-up", which is a convolution of PINUD with an exponential decay function, represented by

$$\mathrm{PINUD}_{\mathrm{buildup}}(t) = \int_{-\infty}^{t} \mathrm{PINUD}(t_0)\exp\left(\frac{t_0 - t}{\tau}\right) dt_0. \quad (1)$$

Various values of the time constant τ were tried between 5000–10000 s, and $\tau = 8000$ s was selected in the latest model. Typical light curves of PINUD and $\mathrm{PINUD}_{\mathrm{buildup}}$ are shown in figure 4.

Then, PINUD and $\mathrm{PINUD}_{\mathrm{buildup}}$ were utilized to sort and refer to the Earth occultation data base. We accumulated PIN event data and pseudo event data (for dead-time correction) under the conditions that the target elevation angle from the Earth limb should be $< -5°$. Since the PIN NXB count rate

[2] It is referred as "quick" or "bgd_a" in the Suzaku team. The event FITS files generated with this method are identified by the keyword of `PINUDLCUNIT` in the `METHOD` record of the FITS file header.

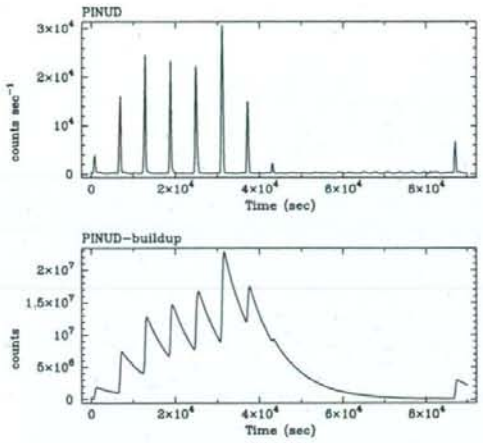

Fig. 4. Example of PINUD-buildup. The top panel shows the light curve of the PINUD count rate in units of counts s^{-1} per one unit (4 PINs), and the bottom shows the $PINUD_{buildup}$ convolved with a time constant of 8000 s.

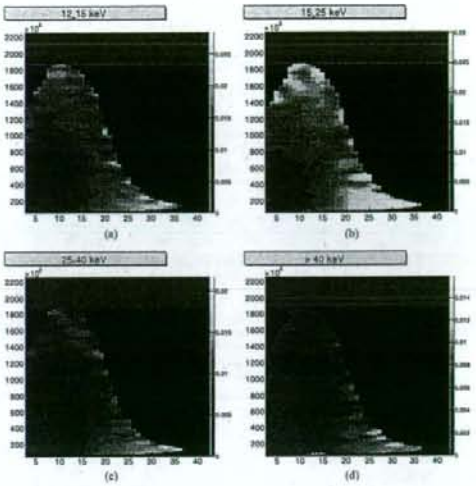

Fig. 5. NXB data base of the `PINUDLCUNIT` method for (a) 12–15 keV, (b) 15–25 keV, (c) 25–40 keV, and (d) > 40 keV. The horizontal and vertical axes are PINUD and $PINUD_{buildup}$, respectively. Color represents the count rate of the PIN NXB.

was affected by the change of bias voltages (500 V to 400 V), and there was a gradual variation of the NXB, the data base was accumulated by considering these issues. There are 16 well-unit counters in the HXD, each of which contains 4 PIN diodes. Since the NXB variation is somewhat different among the units (Kokubun et al. 2007), the data base of each unit is sorted and referred to PINUD and $PINUD_{buildup}$ of the corresponding unit. The data base consists of 40×220 PIN NXB spectra and pseudo events for 4 PINs in each unit. The range of the PINUD in the data base is from 2.5 counts s^{-1} to 42.5 counts s^{-1} per one unit, and that of the $PINUD_{buildup}$ is from 4.0×10^4 counts to 2.25×10^6 counts per one unit. Figure 5 presents an example of the NXB data base divided into four energy bands for visualization. It has been found that the long-term variation of the PIN NXB is significant, and it is not so well reproduced by the data base prepared as mentioned above. Therefore, we correct the total PIN NXB count rate in the data base by a 2nd order polynomial function of time.

The PIN NXB for each observation is estimated by picking up a spectrum from the data base, based on the two parameters. The reference to the data base is performed at each sampling rate of PINUD (2, 4, 8, or 32 s). The exposure of the picked-up spectrum is corrected with dead-time. The time to the next event is determined by the Poisson statistics, based on the total count rate of the NXB spectrum. In order to reduce the statistical error in the number of events in the PIN NXB model, we apply 10 times as high a PIN background rate as the prediction. A pulse height is obtained by generating random numbers, which follow the referred spectrum as a probability distribution. These processes are repeated until the event time passes the end time of each PINUD sampling period, and the process goes to the event generation in the next PINUD sampling period.

This method can generate the NXB model as soon as possible, after the PINUD history becomes available. Therefore, the HXD team supplies the NXB model of this method quickly so that observers can start the analysis at the same time as the data become available. Note that this modeling is not available for the data from 2006 March 23 to 2006 May 13, because of the systematic change of the PIN NXB count rate, as described in section 2.

3.2. *Method Based on Parameterization of Background Light Curve :* `LCFITDT` *(PIN/GSO NXB model)*

The GSO NXB exhibits much stronger variations as a result of activation induced during the SAA passages. These variations are strongly energy-dependent, because many activated nuclei emit various gamma-ray lines together with the continuum. Since the method of simply using the parameter-sorted data base is very difficult to model the GSO NXB, an alternative method is developed, which directly fits the NXB light curves with an empirical model, determines its parameters, and predicts the NXB count rate at any given time. Note that this modeling (`LCFITDT`)[3] can be applied to the PIN NXB as well. In order to reproduce the energy dependence of the background light curve, we model the background separately in 32 energy bands for the GSO NXB. On the other hand, the low count rate of the PIN NXB does not allow us to study the energy dependence of the light curve in detail, and thus we at first model the light curve in the 12–70 keV band, and distribute the count rate in a single 12–70 keV band into 256 energy channels, based on the data base of PIN NXB spectral

[3] This method is referred as "tuned" or "bgd_d" in the Suzaku SWG team. The event FITS files generated with this method are identified by the keyword of `LCFIT` or `LCFITDT` in the `METHOD` record of the FITS file header. Both are basically the same method, but the former does not include the dead-time correction.

shapes, which are sorted by COR[4] and T_SAA_HXD (elapsed time after SAA). However, PIN NXB spectral change would depend on other parameters than the above two parameters, but it is found that the dependence is too small to recognize in the early phase due to low event statistics of PIN NXB, especially for the higher energy band. Therefore, we included such effects after the first-version modeling function is constructed and studied (sub-subsection 3.2.3).

Since the modeling needs the complete PINUD history and the reprocessed gain-calibrated GSO data, the GSO reprocess becomes available after the release of the gain history file for the corresponding observation date, and it is usually 1.0–1.5 months after the pipeline processing. Therefore, the NXB model with the `LCFITDT` method is released after 1.5–2.0 months after the pipeline processing, unlike the `PINUDLCUNIT` method.

3.2.1. Parameterization of the NXB model

In order to study the time variation of the NXB, we accumulate the Earth occultation data, under the following conditions. The target elevation angle should be $< -5°$ (namely, during Earth occultation); the data rate of the Satellite Data Processor (DP) should not be low (L); the in-orbit HXD data transfer should not be saturated; and the COR should be > 6 GV. For the GSO, we divide the accumulated events into 32 energy bands, and derive 200 s bin light curves in each energy band. The boundaries of the 32 energy bands are logarithmically spaced from 53 keV to 1024 keV, with each band having a typical BGD rate of 0.5–1 counts s^{-1}. The PIN light curve is analyzed in a single 12–70 keV energy band.

After the 32 GSO NXB light curves and one PIN NXB light curve are prepared, we fit them individually, with an empirical model to be constructed in the following manner. Like in the modeling method `PINUDLCUNIT`, the PINUD dependence is represented by a term that is a second-order polynomial function of the PINUD counts summed over the 64 PIN diodes. Likewise, the activation component is represented by PINUD build-up counts. In this model, several exponential decay functions with different time constants, τ_k, are considered. The convolution integral is calculated up to 30 τ_k, in order to save calculation time.

Various studies indicate that we need at least 3 or 4 time constants, τ_k, to represent the build-up effects in each energy band. In order to find them, we performed a preliminary analysis. That is, we fitted a whole light curve of the Earth occultation data acquired in the period from 2005 September 2 to 2006 February 28 with a model consisting of the second-order polynomial function of the PINUD counts and the PINUD build-up term with two time constants. Then, we produced confidence contours for the two time constants by scanning them independently. First, we scanned the two time constants in a range shorter than one day, and determined them. After fixing these two short time constants, we newly added two build-up time constants longer than one day, and repeated the search. A shorter time constant was scanned at grid values of 0.5, 0.8, 1.0, 1.5, 2.0, 2.5, 3.0, 4.0, 5.0, 7.0, 10.0, 13.0, 15.0, 18.0, 22.0, 30.0, 45.0, 60.0, 80.0, and 100 ks, while a longer one was scanned over 0.15, 0.25, 0.35, 0.45, 0.55, 0.8, 1.0, 2.0, 3.0, 5.0, 6.5, 8.0, 10.0, 20.0, and 30.0 Ms. Thus, we obtained 4 time constants that describe the PINUD build-up effects in each energy band. The obtained four time constants are typically 1–2 ks, 10–20 ks, a few days, and several tens days, depending on the energy band.

While the activation effects have thus been described approximately by PINUD build-up with four time constants, the modeling is found to be incomplete, mainly due to the following two reasons. We have found that the activation BGD also depends on the angle, θ_B, between the geomagnetic field and the HXD field of view. When θ_B is small, the SAA particles directly enter the tight HXD shield "Wells". As a result, the GSO background count rate due to the activation becomes higher even for the same entrance number of the SAA particles or PINUD build-up count (5%–10% higher when the angle is around 0°). When we included this angle dependence, the background reproducibility was somewhat improved. Apart from the θ_B dependence, there might be other components of activation with time constants other than four time constants included in the model. Such components can be represented by real GSO NXB count rate. Then, we additionally considered the 450–700 keV GSO count rate, $GSOHCNT(t)$, where celestial signals in such energy band are negligible, less than 0.2% even during the Crab observation.

From the above consideration, the empirical model describing the light curve in the i-th energy band is expressed as

$$
\begin{aligned}
&BGD_i(t) = \\
&a_i + \sum_{k=0}^{3} b_{k,i} \int PINUD(t') \cdot \exp\left(-\frac{t-t'}{\tau_{k,i}}\right) dt' \\
&+ \sum_{k=0}^{3} c_{k,i} \left[\int \frac{90° - \theta_B(t')}{90°} \cdot PINUD(t') \cdot \exp\left(-\frac{t-t'}{\tau_{k,i}}\right) dt' \right]^p \\
&+ d_i \cdot PINUD(t) + e_i \cdot PINUD^2(t) \\
&+ f_i \cdot [GSOHCNT(t) - GLC(t)] \cdot \left[1 + g_i \exp\left(-\frac{t - t_{SAA}}{\tau_g}\right) \right] \\
&+ h_i(t) \ , \qquad (2)
\end{aligned}
$$

where the coefficients a_i, $b_{k,i}$, $c_{k,i}$, d_i, e_i, f_i, and g_i are model parameters to be adjusted, and t_{SAA} is the elapsed time from the end of the latest SAA, while $\tau_{k,i}$ are fixed to the values as obtained above and τ_g are fixed to 10000 s, as described later. The index p is 1, except that it is 2 for two shorter time scales of the PIN NXB. The terms with the coefficients, $b_{k,i}$ and $c_{k,i}$, represent the activation, and the term with d_i and e_i represent the PINUD dependence. The term with $f_{k,i}$ and g_i is included to reproduce the activation more accurately with $GSOHCNT(t)$. $GLC(t)$ is a gradually increasing function of the GSO count rate, and is obtained by fitting the light curve of the 450–700 keV band from 2005 August 17 to the current time by the PINUD-build up terms with two long time constants of 0.35 Ms, and 30 Ms. This function subtracts the long-term gradual increase from $GSOHCNT(t)$ so that the GSO count rate only represents the day-by-day background variation that cannot be fully reproduced by other model components. Furthermore, to consider the difference in the time constant of activation between 450–700 keV and other energy

[4] Here we do not use the PINUD, because of technical convenience.

bands, we include the exponential term with a time constant of $\tau_g = 10000$ s, which is found to give a good reproducibility. The last term in this model, h_i, is a correction bias to be explained later, introduced in order to reduce the current uncertainty as much as possible. As a result, input data for modeling the background are *PINUD*(t), *GSOHCNT*(t), $\theta_B(t)$, and t.

3.2.2. Modeling procedure of the GSO NXB

Here we describe the procedure of GSO NXB modeling, based on the model function presented in sub-subsection 3.2.1. The procedure of the PIN NXB modeling is somewhat different, and thus we describe it in sub-subsection 3.2.3, especially for specific issues.

A set of monthly model parameters are determined by fitting the light curve of the Earth occultation data from each month, together with those before and after 10 days of that month. The time region of each fit does not cross any occasion when the HXD operation mode (such as high-voltages and lower discriminator levels) has been changed. After once performing the fit, we exclude data points with large deviations by $>5\sigma$ (σ is a root-mean-square), and perform the fit again to obtain the final parameters. In the fitting, we fix the correction bias, h_i, to 0. Afterwards, we calculate the residual between the background and the model for every 150 ks, and employ the residual as the correction bias, h_i; $h_i(t)$ varies every 150 ks, while the other model parameters are constant during each month. Here, we adapt 150 ks, since the residual on a shorter time scale picks up the Poisson fluctuation, and that on a longer time scale smears out the residual profile. Typically, h_i is at most 0%–2% of the total background. Currently, the number of parameters is still not optimized, and therefore parameter couplings in the light curve fitting sometimes introduce a small discontinuity of the count rate in each component at the month boundary, but the discontinuity is canceled after adding each component.

After the BGD model parameter sets are thus determined for each energy band, we create a background light curve in each energy band at each PINUD sampling time. In this process, we correct the dead-time by using the dead-time light curve estimated from the HXD pseudo event.[5] Finally, BGD events in each band are created, with their pulse heights determined by a Monte-Carlo method while referring to the model-predicted counts in each PINUD sampling period. As shown in figure 6, the pulse height is uniformly and randomly distributed within each energy band of the GSO. Therefore, users should use exactly the same energy boundaries as the present model, when binning the GSO spectra.

3.2.3. Procedure of the PIN NXB modeling

The procedure used to prepare the model of the PIN NXB light curve is the same as GSO NXB, but for only one energy band. The correction factor, $h_i(t)$, is also created in the same way as the GSO NXB model. In order to reproduce the PIN NXB spectrum, the pulse height of each event is generated by random numbers, which follows probability distributions referring to the actual pulse-height spectral data base, accumulated under various values in the COR and T_SAA_HXD; the data base is sorted at boundaries of 6, 7, 8, 9, 10, 11, 12 GV in the COR, and 2000, 4000, 10000 s with respect to T_SAA_HXD. The data base is created from the Earth occultation data during 100 days, centering on each month, together with the condition that the observational set-up of the HXD is the same within each period.

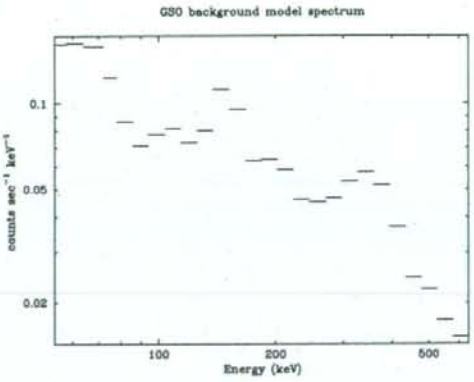

Fig. 6. Example of the GSO background model spectrum.

Although we represent the energy dependence of the PIN NXB light curve as described above, the modeling accuracy is limited because we consider only two parameters to reproduce the energy dependence. The PIN NXB count rate is dominated by events in the lower energy band, and therefore the above modeling is relatively good for this band, but the accuracy becomes worse toward the higher energy band. If the model shows systematic deviations from the real NXB data, and the deviations can be modeled with some appropriate parameters, we can improve the reproducibility of the PIN NXB model. Figures 7 show an example of a comparison of the NXB model with the Earth data against the elevation angle from the Earth rim, the COR, the satellite altitude, and the angle θ_B between the geomagnetic field and the Suzaku field of view. Here, we averaged the Earth occultation data from 2005 September to 2007 August. In a plot against the elevation angle, the blank sky data defined in section 4 were used to cover the elevation above 0°. Systematic residuals of several percent are clearly seen in these figures, but they can be recognized for the first time after long accumulation of the PIN NXB data, because of the low count rate of the PIN NXB, especially in a higher energy band. The residuals against the COR are due to incomplete modeling of the COR dependence by PINUD. Toward the higher satellite altitude, the residuals change positively or negatively in the lower or higher energy band of the PIN NXB, respectively, probably because the particle environment becomes different along the altitude. A negative correlation is seen in the residual against the elevation in the 40–70 keV band; the model tends to overestimate the NXB at larger elevation. Note that the jump at an elevation of 0° is due to the CXB signal above 0°. Since the Earth albedo is at most 0.3% of the PIN NXB, the elevation dependence cannot be explained by it. Perhaps this dependence is thought to be due to secondary particles created

[5] Currently, the GSO NXB model is not corrected by the dead-time, and thus we refer to it as the LCPIT model, to distinguish the dead-time corrected PIN NXB model. In the near future, we will release the dead-time corrected LCPITDT GSO NXB model.

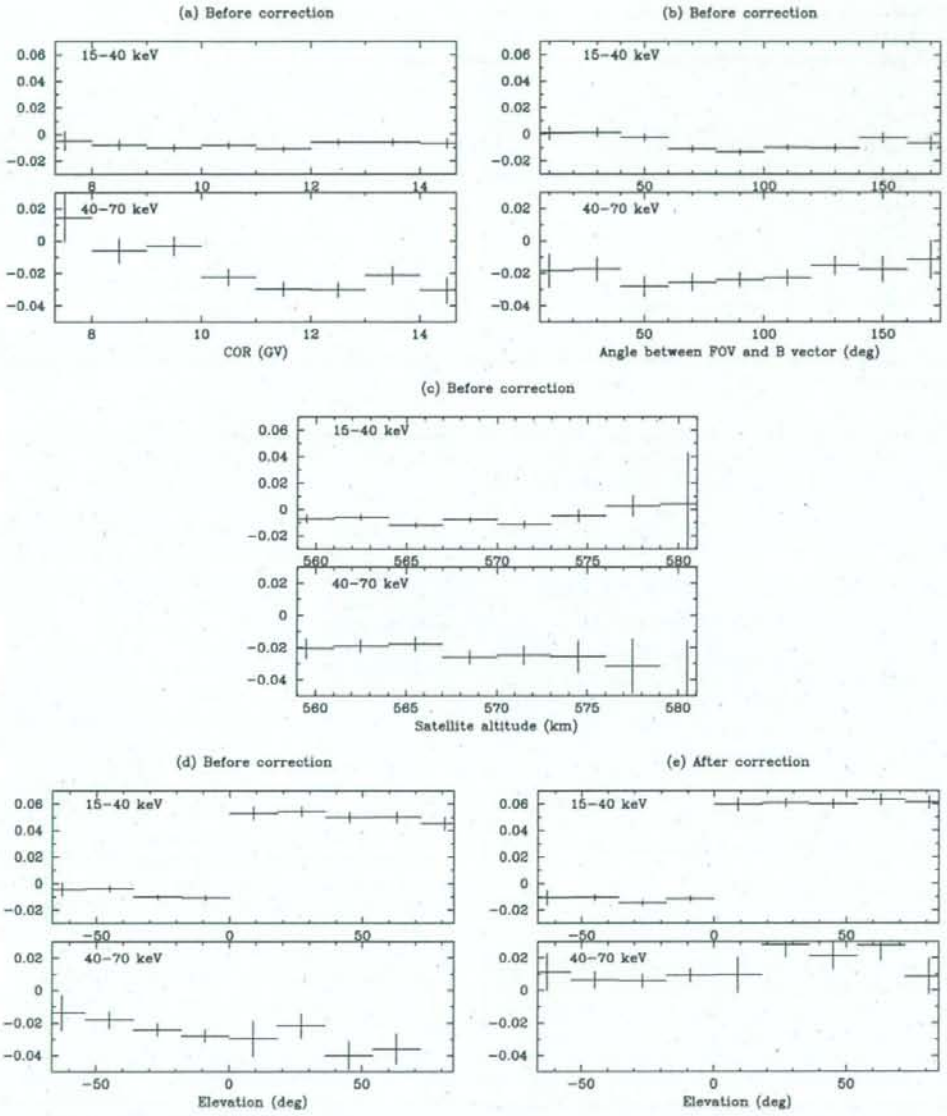

Fig. 7. Residual of PIN background subtraction against (a) COR, (b) θ_B, (c) satellite altitude, and (e) Earth elevation angle before a correction of the background model. Exceptionally, the bottom-right figure (e) shows the residuals against the Earth elevation after a correction of background model.

through the interaction between primary cosmic rays and the Earth atmosphere, and the intensity of the secondary particles is somewhat higher from the Earth side. The residual in the 15–40 keV band becomes larger for θ_B around 30° and 150°, possibly because the effective thickness of the BGO active shield becomes the largest and the NXB becomes smaller for these incident directions.

We then corrected the above systematic dependences against the elevation, satellite altitude, COR, and θ_B. Residual profiles were obtained in the energy range of 15–25, 25–40, 40–70 keV, and were fitted with a 3–5th other polynomial function of the corresponding parameter (COR, elevation ...). The correction factor for arbitrary energy was calculated by linear interpolation between the center energies of 3 energy bands. Even after

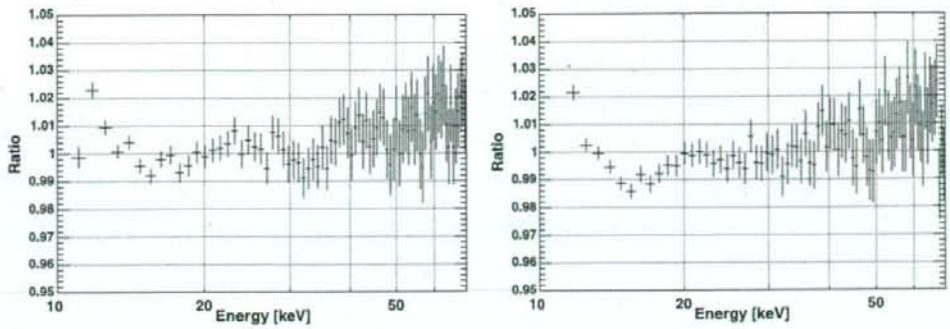

Fig. 8. Ratio of spectra between the data and the background model prediction of all available Earth occultation data (7.9 Ms exposure). Left and right panels show plots for PINUDLCUNIT and LCFITDT, respectively.

that, the comparison of the PIN NXB spectrum between the Earth data and the model had an energy-dependent systematic residual at $\sim 2\%$, and thus we further corrected it by a 4th-other polynomial as a function of energy (the term $K_5(j)$ in the following formula). As a result, we obtained the PIN NXB light curve as:

$$BGD'_j(t) = BGD_{12-70\,\mathrm{keV}}(t) K_1(COR, j) K_2(H_{\mathrm{sa}}, j) K_3(\theta_{\mathrm{elev}}, j) K_4(\theta_B, j) K_5(j) F(j), \quad (3)$$

where j is the pulse-height channel of the PIN event, $BGD'_j(t)$ is the model count rate in the j-th pulse-height channel, $BGD_{12-70\,\mathrm{keV}}(t)$ is the model count rate in the 12–70 keV band corresponding to $BGD_j(t)$ in sub-subsection 3.2.1, H_{sa} is a satellite altitude, θ_{elev} is the Earth elevation, $K_{1,2,3,4}$ is a correction function, and $F(j)$ is a probability function of the pulse height. In figure 7, the residual against the elevation angle for the corrected PIN NXB model is shown, demonstrating that the elevation dependence becomes reduced.

4. Reproducibility of the PIN NXB

4.1. Data Reduction

In this section we examine the reproducibility of the NXB by utilizing the available sky and Earth occultation data from 2005 August 17 to 2008 January 31 for ver 2.0 pipeline processing. The event-selection criteria were the same as those of a cleaned event. To be specific, we applied the following selection criteria:[6] the COR is greater than 6 GV, the elapsed time after the passage of SAA (South Atlantic Anomaly) is more than 500 s and the time to the next entry to SAA passage is more than 180 s, high voltages from all eight HV units have normal values, and the satellite is in the pointing mode and the satellite attitude is stabilized. The elevation angle from the Earth rim is more than 5° or less than −5° for sky and Earth observation, respectively. We also used hxdgtigen to discard the time interval when the telemetry was saturated. Furthermore, the data and background for sky and Earth observations were accumulated within the same good time interval (GTI).

[6] In the Suzaku analysis software, the criteria are given as COR>6 and (T_SAA_HXD>500 and TN_SAA_HXD>180) and (HXD_HV_W[0123]_CAL>700 and HXD_HV_T[0123]_CAL>700) and (AOCU_HK_CNT3_NML_P==1 and ANG_DIST<1.5) and (ELV>5 or ELV<-5).

4.2. Comparison with the Earth Occultation Data

Here, we show the reproducibility of both of the PIN NXB models, by comparing the model with the Earth occultation data. Although the background model is produced based on the Earth data, the modeling is not complete, and therefore it is important to check how the modeling, itself, is accurate, before comparing the model with the sky data. Figure 8 compares the energy spectra between the data and the NXB model during Earth occultation of all available data (7.9 Ms exposure in total). We can see a very good agreement between the model and the data, and can conclude that they agree within $\sim 1\%$ in 15–70 keV for the long-duration averaged Earth occultation data. A small but systematic deviation is seen below 20 keV.

For studying the reproducibility on a shorter time scale, we split the Earth data in each target observation into small pieces with 10 ks exposure and compared the NXB count rate between the data and the model in the 15–40 keV and 40–70 keV range, as shown in figures 9 and 10, respectively; the results are summarized in table 2. We can see that the model reproduces the data in the 15–40 keV region within $\pm 7\%$. In figure 9, it is found that the reproducibility is somewhat worse for the PINUDLCUNIT in such a way that the model count rate is overestimated at a higher background rate, and the data-to-model ratio has a large scatter, and gradually varies with time. More quantitatively, the average of the residual is −0.5% and −0.62% and the standard deviation is 3.75% and 2.31%, whereas the statistical error (1σ) is 1.83%, resulting in systematic uncertainties of 3.27% and 1.40% for PINUDLCUNIT and LCFITDT, respectively. Therefore, the systematic uncertainty of the LCFITDT "tuned" model is less than half that by the PINUDLCUNIT "quick" model, and the statistical error now dominates the residual for the LCFITDT model. We understand that the negative mean of the residual for both models is due to the "dip" around 15 keV in figure 8. On the other hand, the statistical error dominates the residual in the 40–70 keV band: the average of the residual is 1.13% and 0.81% and the standard deviation is 5.53% and 4.92% for PINUDLCUNIT and LCFITDT, respectively, where the

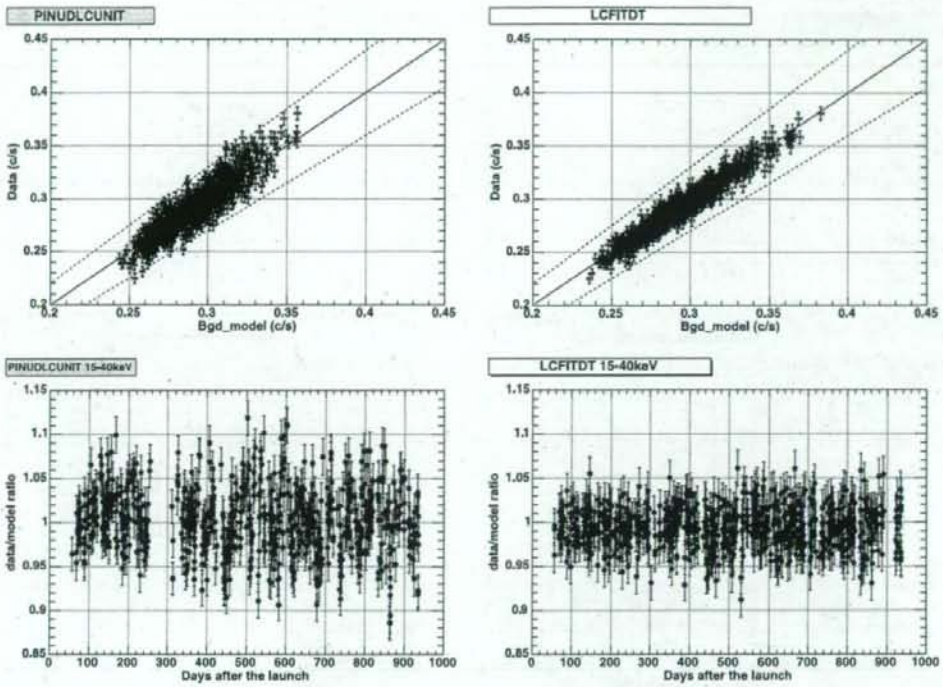

Fig. 9. Comparison of the NXB count rate in the 15–40 keV band between the data and the model prediction. Left and right panels show plots for PINUDLCUNIT and LCFITDT, respectively. Top panels show a scatter plot between the NXB data and the background model. Bottom panels show data to model the ratios of the NXB count rate, plotted against the day since 2005 July 10 (the day of Suzaku launch).

statistical error is 4.03%. Therefore, the standard deviation of the residuals in the high-energy band is dominated by statistical errors.

In order to investigate the reproducibility for the LCFITDT method by avoiding any statistical error, we did the same comparison, but with a longer integration time of 40 ks, as summarized in table 2 and figure 11. As a result, the average, the standard deviation, and the statistical error of the residuals in the 15–40 keV band are −0.58%, 0.99%, and 0.93%, respectively. This results in a systematic uncertainty of about 0.34%. For 40–70 keV, the average of the residual is 0.70% and the standard deviation and the statistical error is 2.87% and 2.03%, respectively, resulting in a systematic uncertainty of about 2.02%, which is comparable to the statistical error.

4.3. *Comparison with the Data of Dark Objects*

In the previous subsection, we confirmed that the background modeling is accurate by several percent for the Earth occultation data. As described in sub-subsection 3.2.3, we consider that the background rate somewhat depends on whether the pointing direction is toward the sky or Earth. Although we include this effect in the model, we must check it. We therefore assess the NXB reproducibility by utilizing the sky observation with no apparent strong hard X-ray objects below.

We first utilized the XIS-FI data to select observations with no strong X-ray emission in the 7–12 keV band (less than 20% above the XIS-FI NXB in entire XIS field-of-view) and compared the HXD-PIN data and the NXB model count rate (10 ks exposure) for 15–40 keV, as shown in figure 12. Here, we plotted the residual histogram in unit of count rate, not the ratio to the NXB model, since we expect a constant excess above 0 due to the CXB emission. The standard deviation (including statistical error) of the residual is about 5.0% and 3.5% of the mean NXB count rate for PINUDLCUNIT and LCFITDT, respectively, which are somewhat larger than that obtained from the Earth occultation data.

One possibility is that the systematic uncertainty increases when observing the sky, but the source confusion limit or fluctuation of the CXB must be considered before making any conclusions. The source confusion limit is estimated from the logN–logS relation in the hard X-ray band. Based on the logN–logS relation obtained with the *INTEGRAL* (Beckmann et al. 2006), the source confusion limit for the PIN field of view becomes 8×10^{-13} erg s^{-1} cm^{-2} (10–50 keV) at the 3σ level, at most 0.08% of the PIN NXB. The CXB sky-by-sky fluctuation was calculated by scaling the HEAO-1 result of 2.8% with the equation $\sigma_{\rm CXB} \propto \Omega^{-0.5} S^{0.25}$ (Condon 1974), where $\Omega = 15.8\,{\rm deg}^2$ and $S \sim 8 \times 10^{-11}$ erg cm^{-2} s^{-1} are the effective solid angle of the observation and the upper cut-off flux

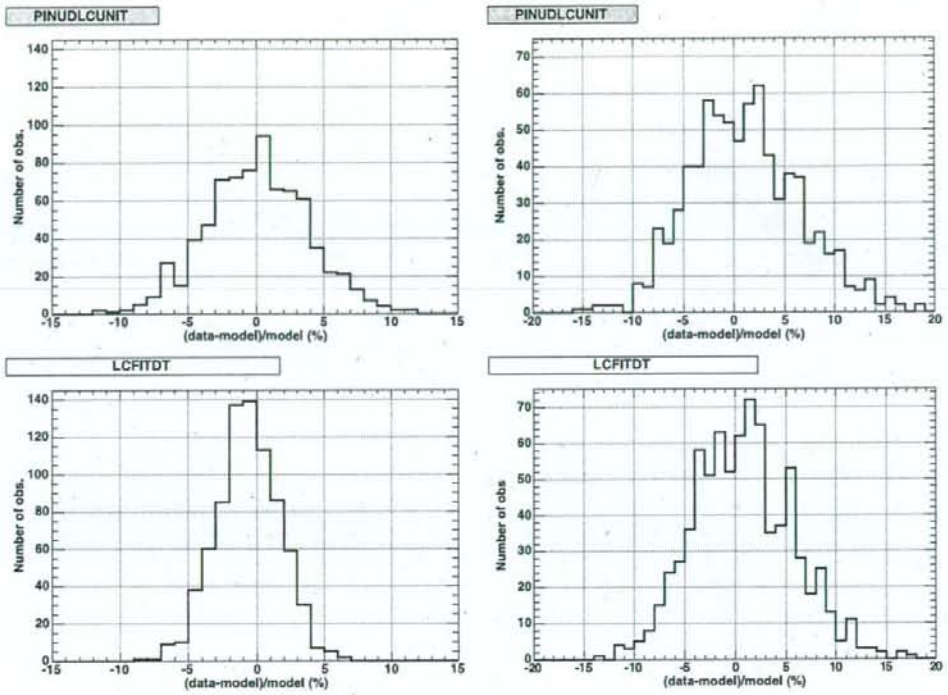

Fig. 10. Histograms of the fractional residual between the NXB data and background model. Top and bottom panels show plots for PINUDLCUNIT and LCFITDT, respectively. Left and right show plots for 15–40 keV and 40–70 keV, respectively.

Table 2. Standard deviation (1σ) of residuals between the PIN Earth data and model.*

15–40 keV	10 ks		20 ks		40 ks	
	PINUDLCUNIT	LCFITDT	PINUDLCUNIT	LCFITDT	PINUDLCUNIT	LCFITDT
Standard deviation (σ)	3.75%	2.31%	3.23%	1.72%	2.96%	0.99%
Statistical error ($\sigma_{\rm stat}$)	1.83%		1.36%		0.93%	
Systematic error ($\sigma_{\rm sys}$)	3.27%	1.40%	2.93%	1.05%	2.81%	0.34%
40–70 keV	10 ks		20 ks		40 ks	
	PINUDLCUNIT	LCFITDT	PINUDLCUNIT	LCFITDT	PINUDLCUNIT	LCFITDT
Standard deviation (σ)	5.53%	4.92%	4.34%	3.51%	3.39%	2.87%
Statistical error ($\sigma_{\rm stat}$)	4.03%		3.01%		2.03%	
Systematic error ($\sigma_{\rm sys}$)	3.78%	2.82%	3.12%	1.81%	2.71%	2.02%

* $\sigma_{\rm sys} = \sqrt{\sigma^2 - \sigma_{\rm stat}^2}$.

of the detectable discrete sources in the field of view, respectively. In the case of the HXD ($\Omega = 34' \times 34'$, and $S \sim 8 \times 10^{-12}$ erg cm^{-2} s^{-1}), the sky-to-sky fluctuation of the CXB was calculated to be 11% (1σ) of the CXB flux, and therefore may not affect the reproducibility of the NXB, since the 1σ CXB fluctuation corresponds to at most $\sim$0.7% of the PIN NXB, and then a larger standard deviation of the residual between data and model for the sky observation is not fully resolved. As a result, the standard deviation for 10 ks sky observations for the PIN 15–40 keV band becomes 2.9%, after subtracting the contribution of the statistical error and the CXB fluctuation. This is still larger than that for the Earth data. Therefore, the reproducibility of the NXB model seems to be worse for sky observations, but one possibility is that the data selection based on the XIS could include the source with $>$0.2 mCrab (2% of the PIN NXB in 15–40 keV), and that such data could contribute to the standard deviation.

In order to avoid the possible CXB fluctuation sky by

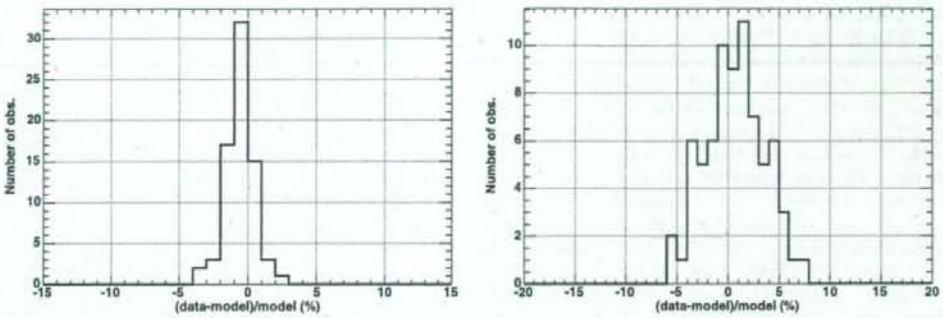

Fig. 11. Same plots for the LCFITDT as those of figure 10, but the integration time is 40 ks instead of 10 ks. Left and right show plots for 15–40 keV and 40–70 keV, respectively.

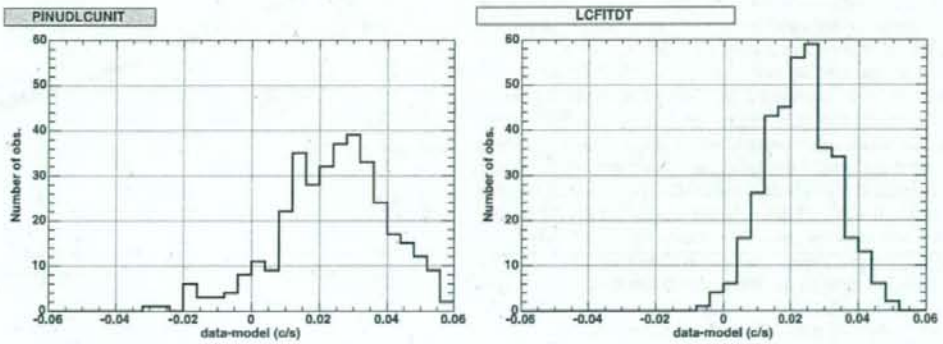

Fig. 12. Histogram of the residual count rate in 15–40 keV between the data and the NXB model for sky observations with a 10 ks integration time. Observations with no apparent hard X-ray objects in XIS FOV are selected (see text for details of the data selection). Left and right panels show plots for PINUDLCUNIT and LCFITDT, respectively.

sky and source confusion observation by observation, we utilized the data of objects that had been repeatedly observed. Figure 13 shows a comparison between the sky data and the NXB model for the SNR E0102.2−7219 observations, in which the same region of the sky was observed regularly for the purpose of XIS calibration. The X-ray emission from this source is thought to be constant and dark for the HXD-PIN, but some observations do not satisfy the selection criteria written at the beginning of this subsection, possibly due to sources or diffuse emission in the SMC within the XIS field-of-view, as reported by Takei et al. (2008). A different roll angle of the field of view against the SMC may also cause a difference in the count rate among observations. Yet, we used all E0102.2−7219 observations in order to compare sky data and the NXB model of as many observations as possible. We also plotted the data and the NXB model of the Cygnus Loop multi-pointing observations in red. These observations were performed for the XIS calibration and cover the regions within 1°.5 in radius, and thus the CXB fluctuation within the field of view of the HXD-PIN can be reduced.

We can see a clear difference in the residual between two sets of observations. The difference of the residuals between two

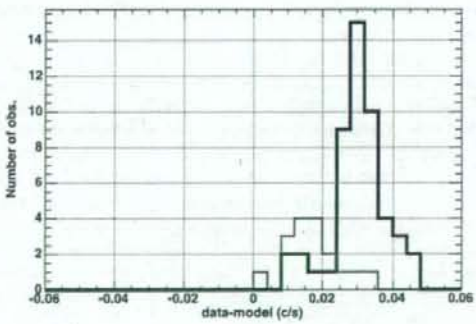

Fig. 13. Same as figure 12, but observations of E0102 (black) and Cygnus Loop multi-pointing (red) are used and results for the background model LCFITDT are shown.

data sets by 0.01–0.015 counts s^{-1} could be due to a weak hard X-ray emission inside the PIN field of view of E0102.2–7219 observations. We looked at a Swift / BAT archival image,[7] but no significant sources with 0.3 mCrab (0.02 counts s^{-1} for PIN) were found. Since this region is in the SMC, many candidates of hard X-ray sources exist, and a sum of their flux would explain the above excess flux.

From figure 13, the residual for E0102.2–7219 data concentrates around 0.03 counts s^{-1} with a narrower width than that for all the dark objects in figure 12, but a few observations show an extraordinary small residual below 0.01 counts s^{-1}. The standard deviation of the residual, including statistical errors, is 0.0080 counts s^{-1} and 0.0077 counts s^{-1} (2.7% and 2.6% of the mean NXB rate) for E0102.2–7219 and Cygnus Loop, respectively. This is smaller than that obtained from many dark observations, but somewhat larger than that for Earth observations. Three data points below 0.015 counts s^{-1} for E0102.2–7219 are from observations on 2007 February 10–11, and thus the NXB accuracy is not good around this observation. As noted in section 6, it was found that the NXB model accuracy is not good for specific periods. In addition, four Cygnus Loop observations were performed in 2006 May, when the background accuracy was relatively worse because the HXD operation mode was changed several times (subsection 2.2). When excluding these data, the standard deviation became 2.3% and 2.1% of the mean NXB rate for E0102.2–7219 and Cygnus Loop, respectively, and these values are almost similar to that for the Earth observations. Therefore, the PIN NXB background accuracy is almost the same between the Earth and sky observations in most cases. We return to this issue in section 6.

Next, we consider the accuracy of background-subtracted spectra by referring to the CXB. If we assume that the Cygnus Loop regions are free from any weak hard X-ray emission, we can regard the averaged spectrum as a sum of the CXB plus the NXB. The NXB-model-subtracted spectrum is compared with the spectrum of the CXB model by Boldt (1987) in figure 14. We can see a very good agreement between the subtracted spectrum (green crosses) and the CXB model (blue ones) within 1% error.

In order to check the NXB reproducibility in a single observation, we also compared the spectrum and the light curve of objects whose signal is expected to be negligible for the HXD-PIN. Examples of comparisons of spectra are shown in figure 15 left. The background-subtracted spectrum and the CXB model by Boldt (1987) are given in blue and green histograms, respectively. No systematic difference can be seen between them up to 60 keV. Figure 15 right also compares the light curves between the data and the NXB model in 15–40 keV band with a time bin of 10 ks. The residuals are consistent with the CXB level in $\pm\sim0.02$ counts s^{-1}, or $\sim$7% of the total NXB count rate.

5. Reproducibility of the GSO NXB

5.1. *Data Reduction*

The data reduction is almost the same as the check of the PIN NXB, but we discard the period when the total GSO count rate is less than 15 counts s^{-1}. Such a low count rate occurs when only 1/4 of GSO data are output to the telemetry for reducing the data size, usually during the data rate L (usually during SAA, low COR period, or earth occultation). However, this 1/4 mode sometimes continues even during the regular observation period,[8] and becomes contained in a clean event. The background model does not support such a mode.

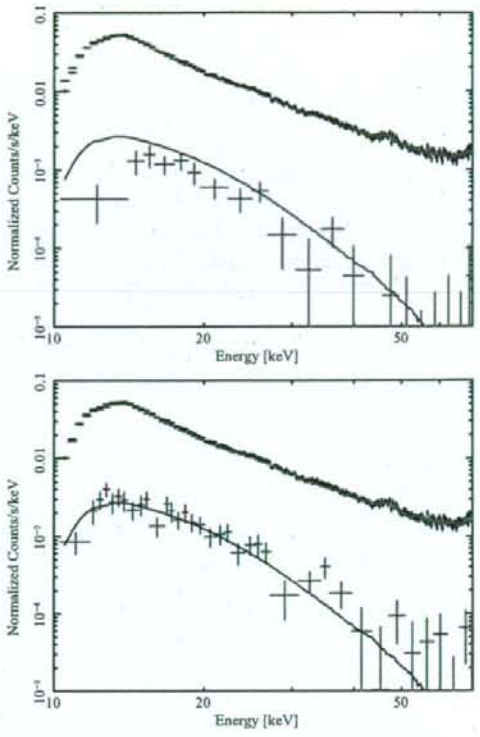

Fig. 14. Averaged spectra of sky observations (black) and the NXB model (red) of Cygnus Loop multi-pointing observations, together with the subtracted spectrum (green) and the CXB model (blue) by Boldt (1987). Top and bottom panels show plots for `PINUDLCUNIT` and `LCFITDT`, respectively.

5.2. *Comparison with the Earth Occultation Data*

Each observation is divided into several periods during which the exposure is 10 ks. When the exposure of Earth occultation within one observation is less than 10 ks, we do not use the data. Accordingly, the GSO count in each data set is typically $(4–9)\times10^4$, and thus the statistical error is typically 0.3%–0.5%. In figure 16, we compare the NXB count rates in each data set between the Earth occultation data and the background model in the 50–100 keV and 100–200 keV ranges, against the elapsed day after the Suzaku launch.

Most of the data and the models agree within $\sim$2% with no time dependence, and no significant difference in

[7] (`http://skyview.gsfc.nasa.gov/`).

[8] Data rate is medium or high or superhigh.

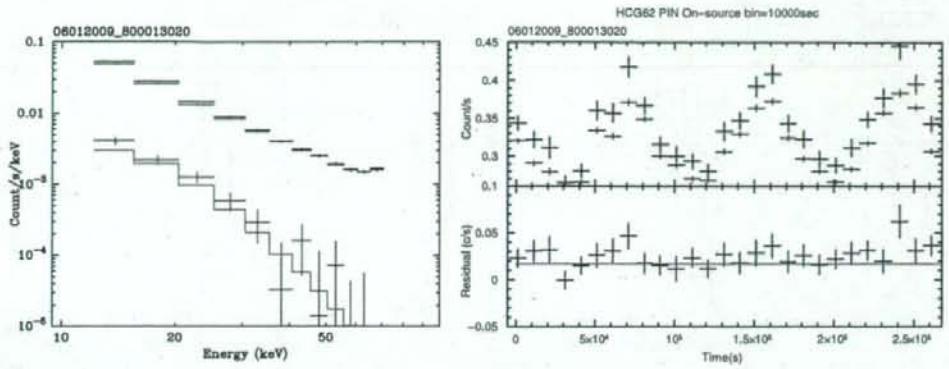

Fig. 15. Left panels are comparisons of spectra between the data (black) and BGD model LCFITDT (red) for observation of HCG 62, which is thought to contain no known strong hard X-rays. Blue cross data points are residuals after the BGD model was subtracted, and the green solid line indicates a typical CXB spectrum. Right figure is a comparison of the light curve in the 15–40 keV band between the data (black) and BGD model LCFITDT (red) for an observation of HCG 62. The bottom panel shows the residuals. A time bin is 10000 s. The horizontal line in the bottom panel indicates the CXB level.

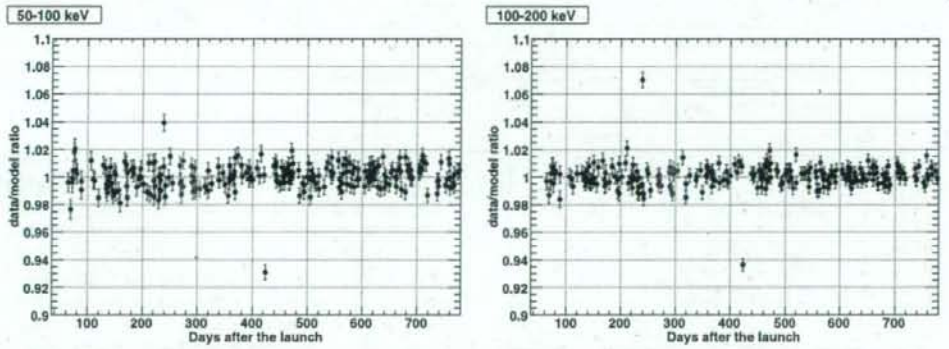

Fig. 16. (Left) Comparison of the NXB count rate in the Earth occultation in the 50–100 keV band between the data and the model prediction. Data from 2006 March 23 to May 13 are shown by green crosses (see text). (Right) The same plot, but for 100–200 keV.

reproducibility is seen between models, even in the period of 2006 March 23 to May 13 during which the GSO LD level was changed. There are some data points that significantly deviate from 1.0 by > 2%, corresponding to observations during which the HXD observation mode is not nominal and the background model cannot be applied. Figure 17 plots the distribution of the NXB count rate ratio between the data and the model prediction. In both energy bands, the distribution is well-represented by a Gaussian with σ values of 0.72% and 0.59% in the 50–100 keV and 100–200 keV bands, respectively. Considering the average of the statistical error of 0.40% and 0.36%, the 1σ systematic errors are estimated to be 0.60% and 0.47% in the 50–100 keV and 100–200 keV bands, respectively. Note that the systematic error depends on the event selection criteria (e.g., COR and energy band) and the integration time. Table 3 summarizes the standard deviation in each energy band as a systematic error. There is an energy band dependency, but the systematic error is less than 1% at 1σ level in any energy band.

Figure 18 top shows a comparison of the spectra for Earth data and the background model, summed over 88 observations of dark objects. The total exposure is 923 ks. It can be seen that the data and model well agree with each other in the whole energy band within 1%.

5.3. *Comparison with the Data of Dark Objects*

In this section, we compare the NXB model with the sky data of dark objects, whose signal is expected to be negligible for the HXD-GSO. Examples of comparisons of spectra for dark objects are summarized in figure 19 left. Unlike the PIN, the CXB is negligible in the GSO band. No systematic difference is seen between the data and BGD model spectra, indicating that the background model is applicable for sky observations. We also compared the data and the NXB model light curves, as shown in figure 19 right for the 50–100 keV band with a time bin of 4000 s. The residuals are mostly within 2% of the total count rate, and we can see some modulations of

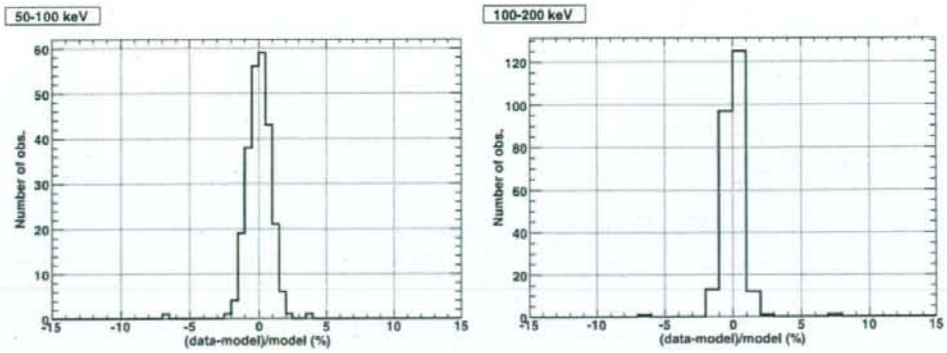

Fig. 17. (Left) Distribution of fractional residual of the NXB count rate between the data and the model prediction in the 50–100 keV band. (Right) The same plot, but for the 100–200 keV band.

Table 3. Standard deviation ($1\,\sigma$) of residuals between the GSO Earth data and model in each energy band.*

	50–100 keV	100–200 keV	200–300 keV	300–500 keV
Standard deviation (σ)	0.72%	0.59%	0.87%	0.71%
Statistical error ($\sigma_{\rm stat}$)	0.40%	0.36%	0.46%	0.34%
Systematic error ($\sigma_{\rm sys}$)	0.60%	0.47%	0.74%	0.63%

* $\sigma_{\rm sys} = \sqrt{\sigma^2 - \sigma_{\rm stat}^2}$.

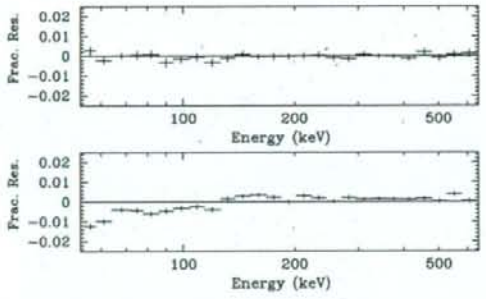

Fig. 18. Fractional residual of the spectra after subtracting the GSO background model from the Earth data (top) and the sky data (bottom), summed over 88 observations of dark objects.

the peak-to-peak amplitude up to ~ 0.1 counts s^{-1} in a cycle of ~ 1 day.

Figure 18 bottom shows a comparison of the spectra for on-source data and background model, summed over 88 observations of dark objects. The exposure is 2430 ks. Although a systematic difference is seen between the data and the model, they agree with each other within 1% in the whole energy band.

6. Cause of Current Systematic Errors of the BGD Model

Although we have developed the background model as accurately as possible, it does not completely reproduce the NXB. This may cause the issues described in subsection 4.3: the background reproducibility is not good for some specific observations. For studying the BGD systematic error related to this issue, it is very useful to investigate the background-subtracted light curve of the count rate for several tens of days. Figure 20 shows light curves of the fractional residual of the count rate after subtracting the background model in the 15–40 keV and 70–100 keV bands for PIN and GSO, respectively. The data of both on-source and Earth-occultation are plotted in different colors for the GSO data. We do not show the on-source data for the PIN, since the PIN data contain the CXB signal and also often the target signal, and they are not useful for studying the BGD systematics. Together with the light curve for a shorter time scale in figure 19, it can be seen that the BGD systematic uncertainty is composed of two components: one with a shorter time scale within 1 day, and the other with a longer time scale of > 1 day. The latter uncertainty appears as a modulation with a time scale of several days in the residual light curve, and its behavior is common between the on-source and Earth data. This behavior is clearly seen for the GSO. For the PIN, the modulation is a less clear, but significant modulation exists at several percent. This trend is also found for the PIN NXB-subtracted light curve around the E0102.2−7219 observation on 2007 February 10–11, leading to a somewhat worse reproducibility, as described in subsection 4.3.

Accordingly, by studying the light curve as above, the background level is more accurately determined than by simply subtracting the background model. As can be seen from the trend in figure 20, the reproducibility is generally worse around an observation during which Earth occultation data are not available for > 1 day. This is because the NXB modeling

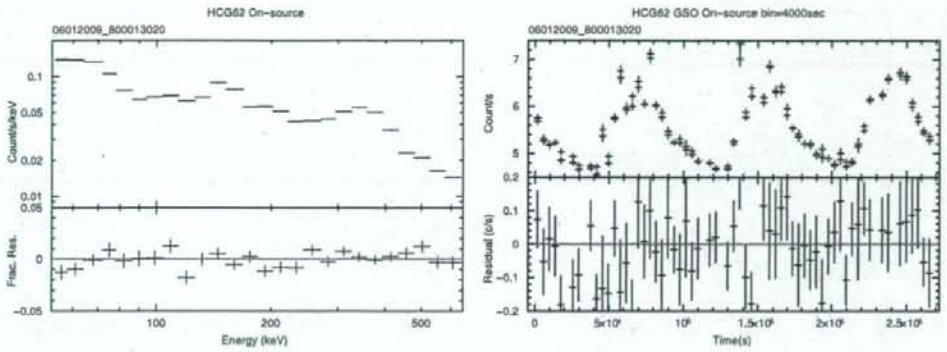

Fig. 19. The left figure is a comparison of spectra between the data (black) and BGD model (red) for observation of HCG 62 whose sky region contains no known strong hard X-rays. Fractional residuals are given by blue crosses in the bottom panel. Right figure is a comparison of the light curve in 50–100 keV between the data (black) and BGD model LCFITDT (red) for observation of HCG 62. The upper panel shows the light curve and the lower panel shows the residual. A time bin is 4000 s.

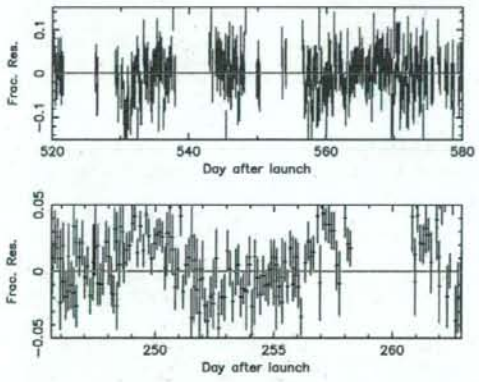

Fig. 20. Light curve of the fractional residual of the count rate after subtracting the background model in the 15–40 keV and 70–100 keV bands for the PIN (top) and the GSO (bottom), respectively. Black and red represent the residual of the on-source data and earth data, respectively.

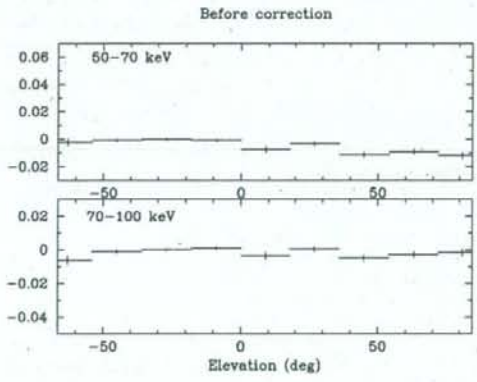

Fig. 21. Residual of GSO background subtraction against the Earth elevation angle.

refers to the Earth data. This trend could be smaller when sky observations with no significant PIN/GSO signal are utilized for NXB modeling. Since the celestial GSO signal is negligible in most observations, the choice of sky observations is not difficult for the GSO NXB modeling. On the other hand, this is not the case for the PIN; the choice of sky observations must be given much attention.

Apart from the above issue, for the GSO NXB, an elevation dependence of $\sim 1\%$ has been found below 70 keV, as shown in figure 21. Although the dependence is very small, we will include such a dependence in the GSO NXB model as the PIN NXB model in the near future. This will improve the systematic negative residual in the low-energy band in figure 18.

7. Current Sensitivity of the HXD

As described in the previous sections, the current HXD NXB modeling achieves 1%–3% reproducibility, but this accuracy depends on the integration time, energy band, period, and so on. Generally, a shorter integration time or a narrower energy band introduces a larger statistical error, and thus the accuracy of NXB subtraction is limited by the photon statistics of the background count rate. Figure 22 shows a comparison of the sensitivity limited by the systematic and statistical errors. Since the PIN NXB count rate is very low, the statistical error becomes dominant for a shorter integration time. On the contrary, the GSO sensitivity is almost determined by the systematic error. Note that this figure represents the sensitivity in a wide energy band, ΔE, of $0.5E$ at a given energy E for

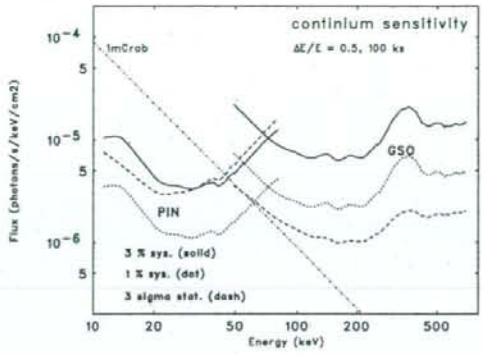

Fig. 22. Continuum sensitivity of the HXD. The solid and dotted lines represent the sensitivity limited by the systematic error of the NXB modeling at 3% and 1% accuracy, respectively. The dashed line represents the sensitivity limited by the statistical error for a 100 ks observation.

a 100 ks exposure. In the spectral analysis, the spectral bin size often corresponds to a narrower energy band, and thus the statistical error in each spectral bin is larger. Furthermore, the PIN sensitivity is also dependent on the CXB sky-to-sky fluctuation, which is a similar level to the current PIN NXB reproducibility.

8. Summary

We modeled the HXD PIN/GSO NXB by utilizing several parameters, including the particle monitor counts and satellite orbital/attitude information. The current reproducibility of the NXB model is estimated to be less than 3% (PIN 15–40 keV) and 1% (GSO 50–100 keV) for more than a 10 ks exposure. The reproducibility is generally worse around an observation during which no Earth occultation data are contained.

The authors wish to thank all members of the Suzaku Science Working Group, for their contributions to the instrument preparation, spacecraft operation, software development, and in-orbit calibration. This work is partly supported by Grants-in-Aid for Scientific Research by the Ministry of Education, Culture, Sports, Science and Technology of Japan (1479206 and 1479201).

References

Beckmann, V., Soldi, S., Shrader, C. R., Gehrels, N., & Produtt, N. 2006, ApJ, 652, 126
Boldt, E. 1987, in IAU symp. 124, Observational Cosmology, ed. A. Hewitt, G. Burbidge, & L. Z. Fang (Dordrecht: Reidel), 611
Churazov, E., et al. 2007, A&A, 467, 529
Churazov, E.,Sazonov, S., Sunyaev, R., & Revnivtsev, M. 2008, MNRAS, 385, 719
Condon, J. J. 1974, ApJ, 188, 279
Frontera, F., et al. 2007, ApJ, 666, 86
Hayashida, K., et al. 1989, PASJ, 41, 373
Imhof, W. L., Nakano, G. H., & Reagan, J. B. 1976, J. Geophys. Res., 81, 2835
Jahoda, K., Markwardt, C. B., Radeva, Y., Rots, A. H., Stark, M. J., Swank, J. H., Strohmayer, T. E., & Zhang, W. 2006, ApJS, 163, 401
Kokubun, M., et al. 1999, IEEE Trans. Nucl. Sci., 46, 371
Kokubun, M., et al. 2007, PASJ, 59, S53
Mitsuda, K., et al. 2007, PASJ, 59, S1
Sazonov, S., Churazov, E., Sunyaev, R., & Revnivtsev, M. 2007, MNRAS, 377, 1726
Takahashi, T., et al. 2007, PASJ, 59, S35
Takei, D., Tsujimoto, M., Kitamoto, S., Morii, M., Ebisawa, K., Maeda, Y., Miller, E. D. 2008, PASJ, 60, S231
Tawa, N., et al. 2008, PASJ, 60, S11

Nuclear Instruments and Methods in Physics Research A 598 (2009) 591–597

Contents lists available at ScienceDirect

Nuclear Instruments and Methods in Physics Research A

journal homepage: www.elsevier.com/locate/nima

Development of a low-noise, two-dimensional amplifier array

Tetsuichi Kishishita [a,b,*], Hirokazu Ikeda [a], Takuto Sakumura [c], Ken-ichi Tamura [a,b], Tadayuki Takahashi [a,b]

[a] Institute of Space and Astronautical Science, Japan Aerospace Exploration Agency, Sagamihara, Kanagawa 229-8510, Japan
[b] Department of Physics, The University of Tokyo, Bunkyo, Tokyo 113-0033, Japan
[c] RIGAKU Co., Ltd., Akishima, Tokyo 196-8666, Japan

ARTICLE INFO

Article history:
Received 21 April 2008
Received in revised form
12 August 2008
Accepted 24 September 2008
Available online 17 October 2008

Keywords:
ASIC
VLSI
Analog front-end
Low noise
CdTe
X-ray
Gamma-ray

ABSTRACT

This paper describes the recent development of a low-noise, two-dimensional analog front-end ASIC for hybrid pixel imaging detectors. Based on the Open-IP LSI project, the ASIC is designed to meet a low-noise requirement of better than 100e⁻ (rms) with self-triggering capability. The ASIC is intended for the readout of pixel sensors utilizing silicon (Si) and cadmium telluride (CdTe) as detector materials for spectroscopic imaging observations in the X-ray and gamma-ray regions. The readout chip consists of a 4 × 4 matrix of identical 270 μm × 270 μm pixel cells and was implemented with TSMC 0.35-μm CMOS technology. Each pixel cell contains a charge-sensitive amplifier, pole-zero cancellation circuit, shaper, comparator, and peak hold circuit. Preliminary testing of the ASIC achieved an 88e⁻ (rms) equivalent noise charge and a 25e⁻/pF noise slope with power consumption of 150 μW per pixel.

1. Introduction

The development of hybrid pixel detectors for particle detection with high spatial resolution in high energy physics experiments has spun off a number of developments with applications in imaging, most notably biomedical imaging, and also imaging in X-ray astronomy. Particularly, in high-energy astrophysics, the hard X-ray imagers that can reconstruct hard X-ray images originating from astronomical point sources with high spatial and high energy resolution at a moderate data rate are the focus of development in studying the non-thermal universe.

So far, cadmium telluride (CdTe) pixel detectors, with high stopping power and good energy resolution, are one of the principal detector materials for the next-generation hard X-ray imager. The hard X-ray imager consists of a super-mirror hard X-ray telescope and CdTe pixel detectors on a focal plane [1]. A two-dimensional readout ASIC assembled with CdTe pixel detectors using the stud-bump technique provides a signal processing circuit for each pixel of the detector. To take advantage of the mirror, the readout ASIC must meet several requirements as follows: (a) low-noise performance better than 100 electrons (rms) with self-trigger capability and a timing resolution of a few tens of microseconds, (b) pixel size of about 250 μm × 250 μm to assemble with CdTe pixel detectors, and (c) low power consumption of about 200 μW per pixel to comply with a limited power budget. Thus, a two-dimensional readout ASIC with excellent spectroscopic performance is a key element for hard X-ray imagers.

In the past few years, we developed several prototype ASICs to establish circuit designs and readout architectures in the Open-IP LSI project led by JAXA (see Ref. [2]). As the first step of prototyping, we developed a 32 × 32 two-dimensional analog ASIC with TSMC 0.25-μm CMOS technology [3,4]. Each pixel cell contains a charge-sensitive amplifier (CSA), three-stage shaping amplifiers and comparator circuits, with special care taken in the layout to set the circuits in pixel cells of 200 μm × 200 μm. In the preliminary tests of the ASIC, we demonstrated a two-dimensional pixel readout scheme and obtained a mean noise level of 279e⁻ (rms) with power consumption of 110 μW per pixel [5].

We subsequently fabricated an eight-channel low-noise analog ASIC with TSMC 0.35-μm CMOS technology [6]. The main objective for the ASIC is to construct a set of verified designs of circuit blocks to be used for two-dimensional ASICs and establish a low-noise architecture. In the performance measurements, we obtained an equivalent noise level of 130e⁻ (rms) and an energy resolution of 2.4 keV for 60 keV gamma rays with a CdTe diode detector [7].

* Corresponding author at: Institute of Space and Astronautical Science, Japan Aerospace Exploration Agency, Sagamihara, Kanagawa 229-8510, Japan.
E-mail address: kisisita@astro.isas.jaxa.jp (T. Kishishita).

0168-9002/$ - see front matter © 2008 Elsevier B.V. All rights reserved.
doi:10.1016/j.nima.2008.09.043

In order to improve the analog performances of the two-dimensional ASIC [5], we developed a new 4 × 4 two-dimensional analog ASIC by utilizing the low-noise circuit architecture of the one-dimensional ASIC [6]. Our objective mainly places emphasis on achieving good energy resolution from detectors in the energy range of 10–80 keV, with a typical counting rate less than 100 cnt/s per pixel. The ASIC is designed to meet a low-noise requirement of better than 100e^- (rms) with a detector capacitance of 1 pF, self-triggering capability, and a power consumption of 150 μW per pixel.

This paper reports the design and preliminary test results of our low-noise, two-dimensional readout ASIC. Section 2 describes the basic structure of the ASIC and details the circuit schematics. Although the circuit architecture in the shaper circuit is the same as in the previously developed low-noise ASIC [6], we employed a transfer gate-type FET as a feedback component in the CSA circuit, which is not employed in the previous ASIC, and also included a pole-zero cancellation (PZC) circuit. Section 3 presents the setup of the performance measurements. Section 4 gives the preliminary experimental results of the ASIC. Finally, Section 5 gives a summary and conclusion.

2. Circuit description

2.1. Overview of the ASIC

The readout ASIC is implemented with TSMC 0.35-μm CMOS technology and has a chip size of 2.95 mm × 2.95 mm. In the ASIC, 16-channel pixel cells of 270 μm × 270 μm are arranged in a 4 × 4 matrix. Fig. 1 shows a photograph of the ASIC. Each pixel cell has a bonding pad area of 40 μm × 40 μm for assembly with a pixel detector. The peripheral circuits contain bias circuits and shift registers used for pixel selection (Fig. 2). Among the 16 channels, the outer four pixel cells are connected to bonding pads and the other 12 channels are isolated. These four channels can be used for evaluating spectral performance when connected to the Si and CdTe detectors. The power consumption in each pixel cell is

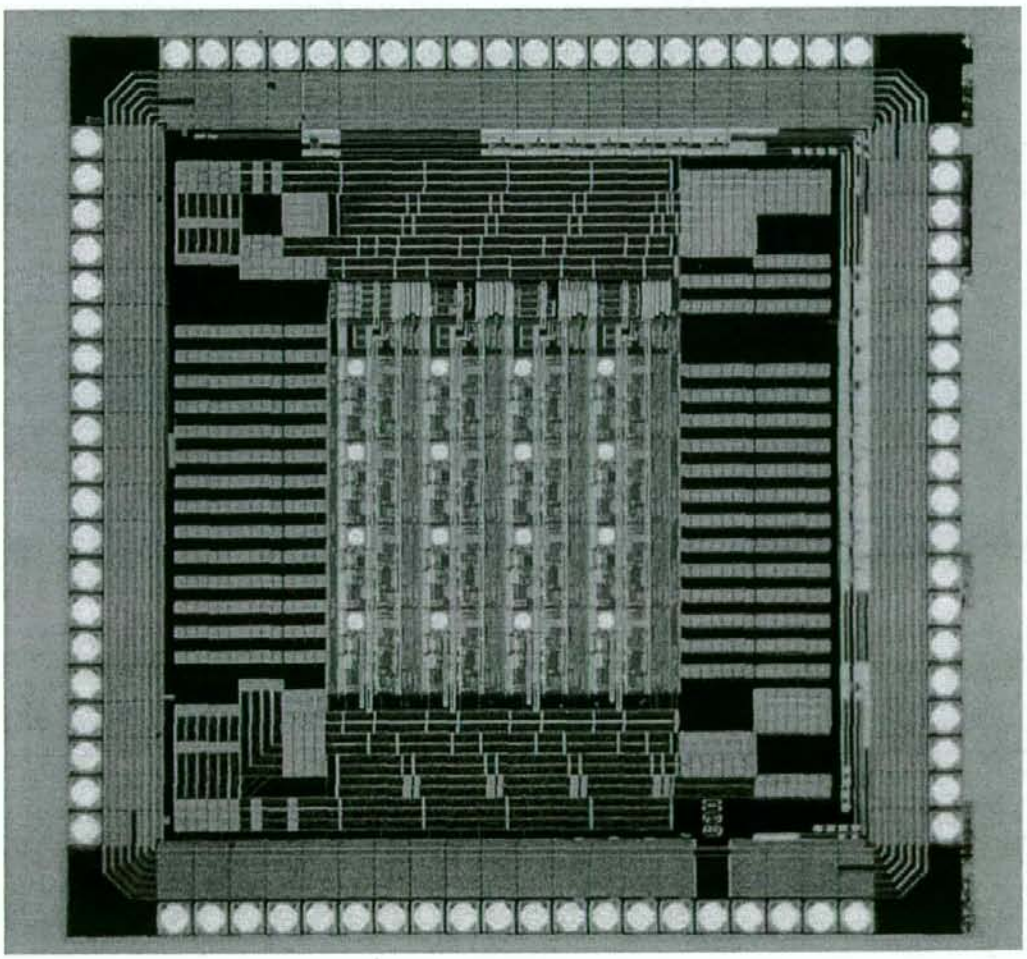

Fig. 1. Photograph of the two-dimensional ASIC. The chip size is 2.95 × 2.95 mm^2 with 16-channel pixel cells of 270 × 270 μm^2 arranged in a 4 × 4 matrix. Each pixel cell has a bonding pad for assembling with a pixel detector.

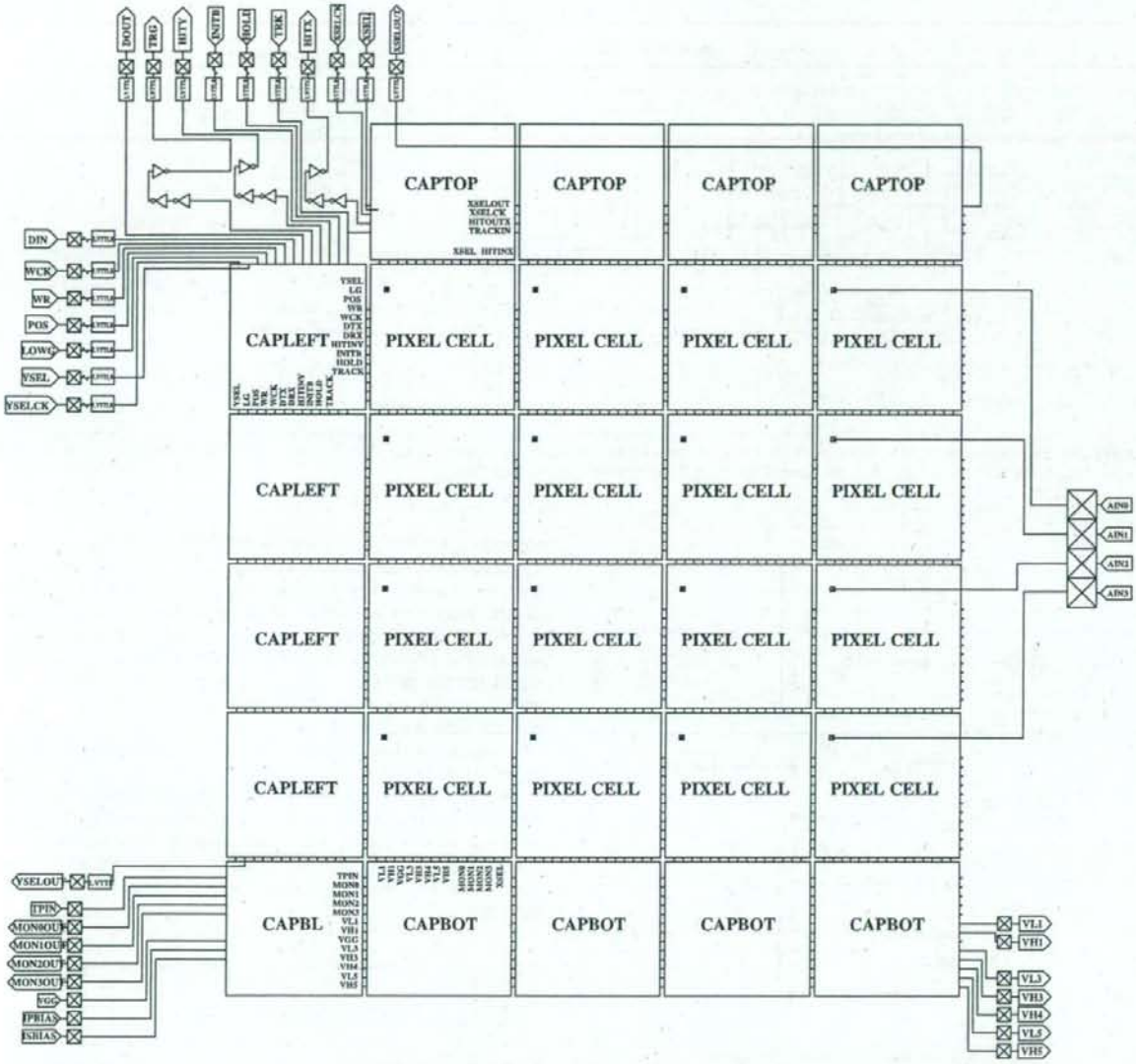

Fig. 2. Block diagram of the ASIC. Bias voltages are supplied from the bottom module. Shift registers used for pixel selects are contained in CAPTOP and CAPLEFT modules. Analog inputs of the outer four pixel cells are connected to bonding pads.

Table 1
Overview of the ASIC

Fabrication process	TSMC 0.35-μm CMOS
Chip size	$2.95 \times 2.95\,mm^2$
Number of channels	16
Pixel size	$270 \times 270\,\mu m^2$
Power consumption in each pixel	150 μW
Total power consumption	9.9 mW
Power rail	±1.65 V

150 μW and the total power consumption including the peripheral circuits is 9.9 mW for the power rails of ±1.65 V. LVDS digital signals are used to control the ASIC (Table 1).

2.2. Analog processing

Fig. 3 shows the analog circuit in a pixel cell. The signal processing chain consists of a CSA, PZC circuit, shaper, comparator, and peak hold circuit. To achieve lower power consumption and plug into a limited pixel space, we modified the overall architecture in comparison with the previous ASIC designs [6]. The key changes are as follows: (a) two shaper circuits with different shaping time constants are unified to a common circuit, (b) CMOS switches are inserted in front of the buffer circuits provided for monitoring analog output signals (with the switches activated only when the monitor pixel is selected), and (c) ESD protection circuits were not employed at CSA inputs.

Fig. 4 shows the schematic of the preamplifier circuit employed for the CSA. The preamplifier circuit is based on a